*Progress In Electromagnetics Research, PIER 96, 173–191, 2009*

# A FULLY-ADAPTIVE SMART ANTENNA PROTOTYPE: IDEAL MODEL AND EXPERIMENTAL VALIDATION IN COMPLEX INTERFERENCE SCENARIOS

**M. Benedetti, G. Oliveri, P. Rocca, and A. Massa**

Department of Information Engineering and Computer Science
University of Trento
Via Sommarive 14, I-38050 Trento, Italy

**Abstract**—In this paper, the architecture of a smart antenna prototype is described and its functionality assessed. The system prototype is composed by an 8-elements linear array of dipoles with a finite reflecting plane and the adaptive behavior is obtained modifying a set of array weights with electronically-driven vector modulators. In order to real-time react to complex interference scenarios, the system is controlled by a software control module based on a Particle Swarm Optimizer. To demonstrate the feasibility and the effectiveness of the proposed implementation, a set of representative results concerned with different interference scenarios is reported and discussed.

## 1. INTRODUCTION

Thanks to the development of wireless technologies, mobile communication devices have known a wide diffusion in the last decade. To properly deal with complex scenarios characterized by multiple users as well as different standards, communication systems that allow a suitable quality of service (QoS) and an enhanced security are needed [1]. In this framework, smart antennas [2–4] have been recognized as promising tools for an efficient management of the physical layer. Such systems usually consist of an antenna array and a signal processing module to real-time maximize the quality of the communication evaluated (at the physical layer) in terms of signal-to-interference-plus-noise ratio (*SINR*) at the receiver. Towards this end, smart antennas steer the main lobe of the beam pattern to track the desired signal and cancel the interferences determining suitable attenuation values along the

Corresponding author: A. Massa (andrea.massa@ing.unitn.it).

jammers directions. As a consequence, the channel capacity and the service coverage turn out to be increased with respect to standard solutions [5]. On the other hand, thanks to their reconfigurability, smart antennas have been also employed in multiple-input multiple-output (MIMO) wireless systems [6, 7].

Although the effectiveness of a hardware implementation has been theoretically proved [8], the technological difficulties and costs for the implementation of fully-adaptive solutions prevented a widespread application of smart antennas in wireless communications. As a matter of fact, simpler architectures have been usually considered (e.g., reconfigurable parasitic antennas or switched beam antennas [9]). As far as parasitic architectures are concerned, several prototypes have been implemented by exploiting the theoretical basis of the functioning of the Uda-Yagi antennas [10, 11] (i.e., a single active antenna whose pattern is shaped by means of a set of real-time controlled parasitic elements). Despite compact sizes and low-cost architectures, such devices are not able to steer the position of the pattern nulls in a continuous way, thus limiting the adaptation to the environment of the whole transmission system.

Consequently, some efforts have been devoted to realize a fully-adaptive behavior and more complex prototypes have been built. Some devices have been implemented making use of complex acquisition systems, where the signal is collected at the receiver and at the output of the array elements in order to compute the co-variance matrix [12, 13]. The adopted control strategies are based on the gradient method (e.g., the least mean square algorithm by Widrow [14]) for the minimization of a cost function defined as the error between the received signal and a reference one. On the other hand, simpler fully-adaptive systems based on the measurement of the received signal at the receiver have been also implemented [15]. Such devices are usually controlled by means of heuristic optimization strategies aimed at maximizing a suitable fitness function proportional to the signal-to-interference-plus-noise ratio. In both cases, the effectiveness of the implementation has been assessed by comparing measured and simulated radiation patterns in correspondence with a single interferer incoming from a fixed direction.

This paper discusses the implementation of a fully-adaptive smart antenna devoted to the real-time suppression of multiple jammers and focus on the experimental validation by considering complex interference scenarios. The antenna has already been presented by Azaro et al. [16, 26] and its functionalities have been preliminary assessed by considering a simple experiment [17, 27]. The prototype is characterized by a simple functional scheme where the signals collected

by the array elements are suitably weighted by the hardware control unit according to an iterative strategy based on a customized version of the Particle Swarm Optimizer (PSO) [18] to maximize a suitable fitness function. As far as the validation is concerned, a selected set of experiments characterized by multiple slots of time and different directions of arrival for the interferences is considered. The efficiency of the proposed implementation is analyzed in terms of both the behavior of the signal-to-interference-plus-noise (*SINR*) ratio and the capability of placing nulls in suitable positions of the radiation pattern.

The paper is structured as follows. In Section 2, the behavior of the smart antenna is briefly outlined. Section 3 is concerned with the description of the architecture of the smart antenna. The validation of the prototype is then discussed in Section 4, where a selected set of measurements of the signal-to-interference-plus-noise ratio as well as of the radiation patterns is compared with the results of the numerical simulations. Finally, some conclusions are drawn (Section 5).

## 2. SMART ANTENNA BEHAVIOR

Let us consider a linear array of $M$ equally-spaced elements. At each time-step[†] $t_l$, $l = 1, \ldots, L$, the antenna receives a signal from a desired source and a set of $Q$ interfering sources. The signal collected at the $m$-th element of the array is given by

$$s_m(t_l) = d_m(t_l) + \sum_{q=1}^{Q} u_{q,m}(t_l) + n_m(t_l) \qquad m = 1, \ldots, M \tag{1}$$

where $d_m$ and $u_{q,m}$ denote the contribution of the desired signal and of the $q$-th interference, $q = 1, \ldots, Q$, respectively. Moreover, $n_m$ models the uncorrelated background noise. With reference to Fig. 1, the signal $y(t_l)$ available at the output of the receiver turns out to be

$$y(t_l) = \sum_{m=1}^{M} w_m(t_l)\, s_m(t_l) \tag{2}$$

where $w_m(t_l) = \alpha_m(t_l)\, e^{j\beta_m(t_l)}$ is the $m$-th complex weight at the $l$-th time-step.

As far as the smart behavior of the system is concerned, the weight vector $w(t_l) = \{w_m(t_l);\, m = 1, \ldots, M\}$ is updated at each time-step to react to the continuously (i.e., at each time-step) changing

[†] A time-step is a slot of time, between two consecutive snapshots, characterized by the presence of a desired signal and a fixed number of interfering signals with invariant directions of arrival (DoAs).

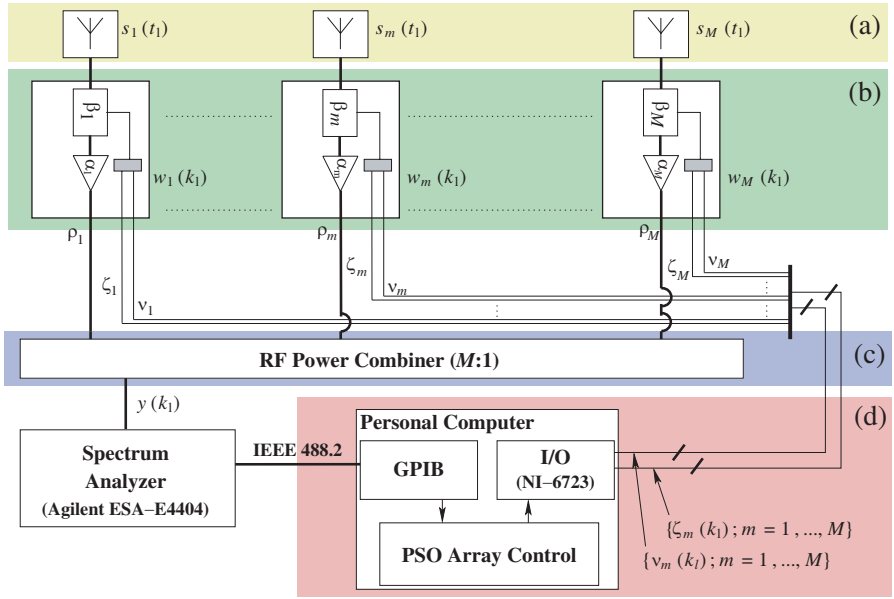


**Figure 1.** Architecture of the fully-adaptive smart antenna prototype. Functional block diagram of the system.

interference/environment conditions, thus maximizing the signal-to-interference-plus-noise ratio (*SINR*) at the receiver. Since the *SINR* is not usually/easily measurable at the receiver, the total power $\Psi^{\text{tot}}(t_l)$ of the output signal $y(t_l)$ is considered [19, 20] as an index of the system performance and the fitness function $\Theta(t_l)$

$$\Theta\left(t_l\right) = \frac{\left|\sum_{m=1}^{M} \alpha_m\left(t_l\right) e^{j\left[\frac{2\pi}{\lambda} x_m \cos\phi^d + \beta_m(t_l)\right]}\right|^2}{\Psi^{\text{tot}}\left(t_l\right)} \tag{3}$$

is maximized to determine the optimal weight vector $w_{\text{opt}}(t_l) = \arg[\max_w SINR\{w(t_l)\}]$ [20]. In (3), $x_m$ is the position of the $m$-th element, $\phi^d$ and $\phi_q^u$, $q = 1, \ldots, Q$, are the directions of arrival (DoAs) of the desired and $q$-th jammer, respectively. For the sake of clarity, the measured value of $\Psi^{\text{tot}}$ is obviously related to the array coefficients according to the following relationship

$$\Psi^{\text{tot}}\left(t_l\right) = \sum_{m=1}^{M} \alpha_m\left(t_l\right) e^{j\beta_m(t_l)} \sum_{i=1}^{M} \alpha_i\left(t_l\right) e^{-j\beta_i(t_l)} \Omega_{i,m}^{\text{tot}} \tag{4}$$

where $\Omega_{i,m}^{\text{tot}}$ is the $(i, m)$-th entry of the co-variance matrix of the

received signal $y(t_l)$ [21].

At each time-step, the arising optimization problem

$$w_{\text{tot}}(t_l) = \arg\left[\max_w \Theta\left\{w(t_l)\right\}\right] \tag{5}$$

is then solved by means of a PSO-driven approach following the implementation guidelines in [18]. More specifically, a swarm of $P$ particles is used to model the trial solutions at each time-step. The swarm samples the solution space in a set of successive iterations, $k_l = 1, \ldots, K_{\max}$ ($k_l$ being the iteration index of the $l$-th time-step) by exploiting the history of the swarm as well as the knowledge of the optimal solutions at the previous steps (i.e., the so-called *swarm memory* $\Pi(t_l) = \{w_{opt}(t_i),\, i = l-1,\, l-2,\, \ldots\}$) until the new time-step ($l \leftarrow l+1$) or when $\Theta\{w(t_l)\} \geq \eta$, $\eta$ being a user-defined convergence threshold [22].

## 3. ARCHITECTURE OF THE SMART ANTENNA

The smart antenna prototype operates as a receiving system in the *ISM* band ($f_c = 2.45\,\text{GHz}$). It is composed by the functional blocks shown in Fig. 1: (3.1) a "Radiating Module" [Fig. 2(a)]; (3.2) a "Hardware Control Module" [Fig. 2(b)]; (3.3) a "Radio-frequency Signals Combiner"; and (3.4) a "Software Control Module" [16, 17]. For the sake of completeness, the architecture of the functional blocks is described in the following subsections.

### 3.1. Radiating Module

The array consists of $M = 8$ ($D = \frac{\lambda}{2}$ being the inter-element distance where $\lambda$ is the free-space wavelength) printed dipoles built following the indications given in [23]. More specifically, the ground plane of the feeding microstrip line and the half-wave dipole strips have been printed on the same plane, while the via-hole balun has been placed on the other side of the FR-4 substrate. With reference to Fig. 2(a), a finite reflecting plane of length $L = 4.5\lambda$ and height $H = \lambda$ has been placed behind and parallel to the dipoles at a distance $W = 0.25\lambda$ from their arms.

### 3.2. Hardware Control Module

The HW Control Module is composed by a set of $M$ AD8341 Analog Device RF vector modulators [24] that weight the signals $s_m(k_l)$, $m = 1, \ldots, M$, from the array elements with the coefficients $w_m(k_l)$, $m = 1, \ldots, M$, computed by the PSO-driven control. Such a module

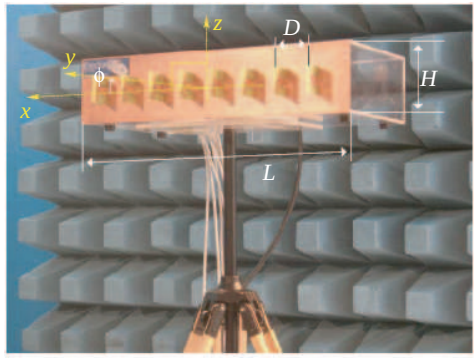


(a)

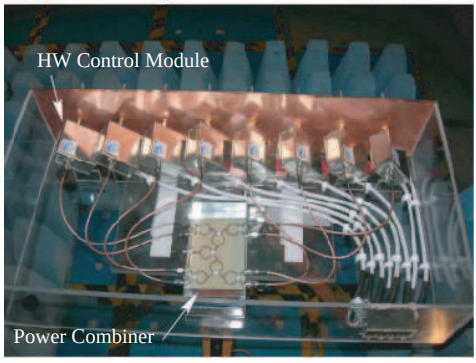


(b)

**Figure 2.** Photographs of the fully-adaptive smart antenna prototype. (a) Front view (*radiating module*) and (b) back view (*HW control module and power combiner*).

has been installed on a FR-4 printed circuit board (PCB) and each modulator is driven by two low-frequency differential signals $\nu_m(k_l)$, $\zeta_m(k_l) \in [-0.5, 0.5\,\mathrm{V}]$ (Fig. 1) to generate a phase shift value $\beta_m$ equal to

$$\beta_m(k_l) = \arctan \frac{\nu_m(k_l)}{\zeta_m(k_l)}, \qquad \beta_m \in [0; 360], \tag{6}$$

and an attenuation given by

$$\alpha_m(k_l) = \sqrt{\zeta_m(k_l)^2 + \nu_m(k_l)^2}, \qquad \alpha_m \leq 0.5 \tag{7}$$

in the range $\alpha_m \in [4.5\,\mathrm{dB}; 34.5\,\mathrm{dB}]$.

### 3.3. Radio-frequency Signal Combiner

The $M = 8$ RF signals coming from the HW Control Module are added, by means of the RF power combiner shown in [Fig. 2(b)], to determine the output signal $y(k_l)$. The combiner is composed by seven Wilkinson devices [25] printed on an Arlon N25 substrate.

### 3.4. PSO-driven Software Control Module

The output signal is then processed by a spectrum analyzer Agilent ESA-E4404 to measure the total output power $\Psi^{\text{tot}}(k_l)$. Such an information is then transferred to the Software (SW) Control Module by means of a GPIB input interface. Concerning the SW Control Module, it consists of a personal computer (PC) where the input/output communication interfaces and a SW unit, which implements the PSO-driven control logic [18], have been installed. At each time step $t_l$, the SW module maximizes the *SINR* by looking for the optimal set $\{[\zeta_m^{\text{opt}}(t_l), \nu_m^{\text{tot}}(t_l)]; m = 1, \ldots, M\}$ of the differential signals (i.e., the corresponding optimal weight configuration, $w_{\text{opt}}(t_l) = \{w_m^{\text{opt}}(t_l); m = 1, \ldots, M\}$, being $w_{\text{opt}}(t_l) = \arg[\max_{p=1,\ldots,P}\Theta\{w_p(k_l)\}]$) that optimizes (3).

## 4. EXPERIMENTAL VALIDATION

This section is concerned with the experimental validation of the smart antenna prototype. Firstly, the results of a preliminary testing and calibration of the prototype will be discussed. Then, the behavior of the prototype in dealing with complex interference scenarios will be described and analyzed in order to assess the feasibility of the adaptive control ad the reliability/effectiveness of the proposed implementation.

### 4.1. Preliminary Calibration and Testing

A preliminary calibration and testing of the prototype has been carried out by comparing, for each functional block, the numerical simulations of the design phase with a set of experimental measurements. For the sake of brevity, the behavior of the HW Control Module and of the whole system in a static configuration is discussed here.

The first validation is concerned with the accuracy of the RF vector modulator in generating the required attenuation and phase shift values. Towards this purpose, let us define the error indexes

$$\Delta = \sqrt{\alpha^2 + \tilde{\alpha}^2 - 2\alpha\tilde{\alpha}\cos\left(\beta - \tilde{\beta}\right)} \tag{8}$$

**Table 1.** *Testing phase* — Error indexes.

| $\nu$ [V] | $\zeta$ [V] | $\alpha$ | $\tilde{\alpha}$ | $\beta$ [deg] | $\tilde{\beta}$ [deg] | $\Delta$ | $\delta$ |
|---|---|---|---|---|---|---|---|
| 0.0 | 0.0 | 0.0 | 0.0102 | 0 | 52.15 | 0.0102 | 0.0102 |
| 0.5 | 0.0 | 0.5 | 0.3793 | 0 | 0.00 | 0.1207 | 0.1207 |
| 0.0 | −0.5 | 0.5 | 0.3715 | 270 | 275.62 | 0.1353 | 0.1285 |
| −0.5 | 0.0 | 0.5 | 0.3890 | 180 | 180.59 | 0.1111 | 0.1110 |
| 0.0 | 0.5 | 0.5 | 0.3737 | 90 | 103.89 | 0.1639 | 0.1263 |

and

$$\delta = |\alpha - \tilde{\alpha}| \tag{9}$$

where the superscript ˜ indicates an experimentally measured quantity. Table 1 summarizes the obtained results in correspondence with a set of representative values of the control signals. As it can be noticed, the error $\Delta$ is lower than 0.17 and such a mismatching between simulated and measured values is mainly due to the approximation of the $\alpha$ coefficient. As a consequence, the weight amplitudes have been fixed to $\alpha_m(k_l) = 0.5$; $m = 1, \ldots, M$; $l = 1, \ldots, L$ and the adaptive control has been obtained by adjusting the phase coefficients $\beta_m(k_l)$.

The second experiment deals with a "static" scenario and it is aimed at assessing the ability of the whole system to reproduce the simulated "quiescent" pattern. Towards this end, the radiation pattern $G(\phi)$ has been measured in a controlled environment (i.e., anechoic chamber) and it has been compared with the corresponding data from the numerical simulation [22]. Fig. 3 shows the pattern generated by setting $w_m = 0.5$, $m = 1, \ldots, M$. As it can be observed, the simulated pattern is carefully matched despite a shift of the angular positions of the nulls. Such a difference is mainly caused by the mutual coupling effects and the presence of the finite reflecting plane. As a matter of fact, the numerical simulator did not model the actual structure of the smart antenna, but an ideal array of point-like ideal radiators.

### 4.2. Validation in Complex Time-varying Scenarios

This subsection is aimed at analyzing the performance of the prototype in a time-varying situation. The results of three experiments concerned with variations on DoAs, interference power, and number of jammers will be presented and discussed. As far as the measurement setup is concerned, the interference sources have been placed in front of the smart antenna along a circular perimeter ($\rho = 28\lambda$) and at different angular positions (Fig. 4).

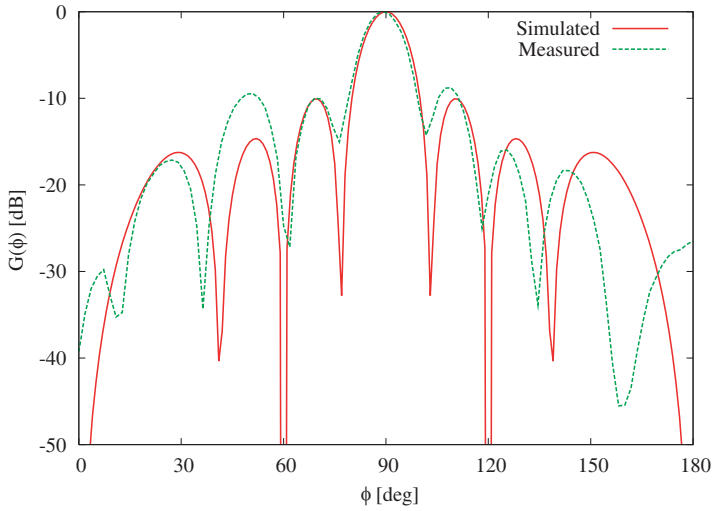


**Figure 3.** *Testing phase* — Quiescent radiation pattern.

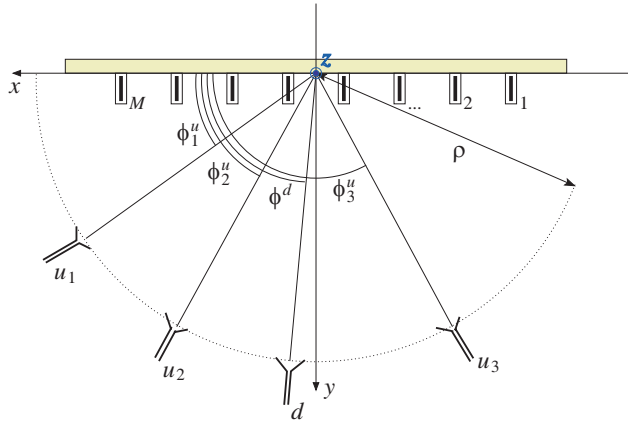


**Figure 4.** *Testing phase* — Sketch of the geometry of the testing setup.

### *4.2.1. Experiment A*

The scenario of the first experiment is concerned with a single interference source ($Q = 1$) whose DoA and power have been varied according to the evolution detailed in Table 2. Moreover, $\phi^d$ has been set to 0 and $\Psi^d = 100\,\mathrm{mW}$.

**Table 2.** *Experiment A* — Description of the interference scenario. Evolution of the *DoA* and power level of the interference signal.

| $l$ | $\Psi^d(t_l)$ [mW] | $\phi^u(t_l)$ [deg] | $\Psi^u(t_l)$ [mW] |
|---|---|---|---|
| 1 | 100 | 69 | 150 |
| 2 | 100 | 111 | 20 |
| 3 | 100 | 132 | 80 |
| 4 | 100 | 111 | 80 |
| 5 | 100 | 99 | 50 |

The obtained results are summarized in Fig. 5 where the behavior of the *SINR* at the receiver versus the iteration index $\chi$ ($\chi \triangleq \sum_{l=1}^{L} k_l$) [Fig. 5(a)] and two representative samples of the radiation pattern [Figs. 5(b)–5(c)] are reported. As for the *SINR* at each iteration $\chi$, it has been computed as follows

$$SINR\,(\chi) = \frac{\tilde{\Psi}^d\,(\chi) - \hat{n}\,(\chi)}{\tilde{\Psi}^u\,(\chi)} \tag{10}$$

where $\tilde{\Psi}^d(\chi)$ and $\tilde{\Psi}^u(\chi)$ are the power of the desired signal and of the undesired one measured when turning off the interference sources [i.e., $u_q(\chi) = 0$, $q = 1, \ldots, Q$] and the desired signal [i.e., $d(\chi) = 0$], respectively. Moreover, $\hat{n}(\chi)$ is the noise level estimated at the $\chi$-

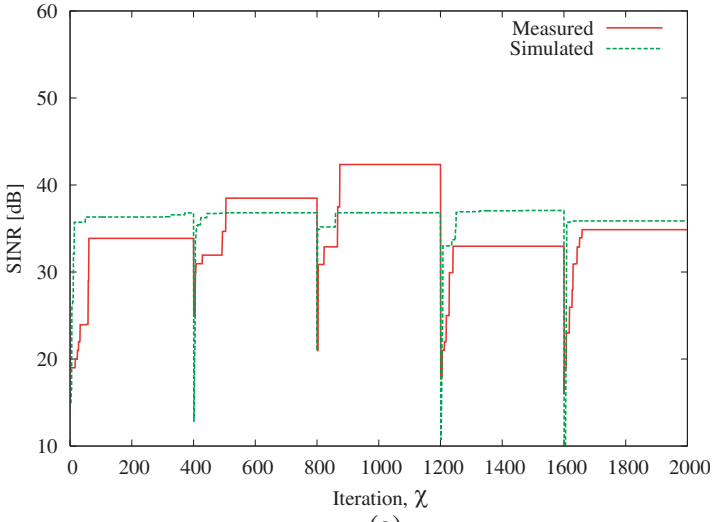

(a)

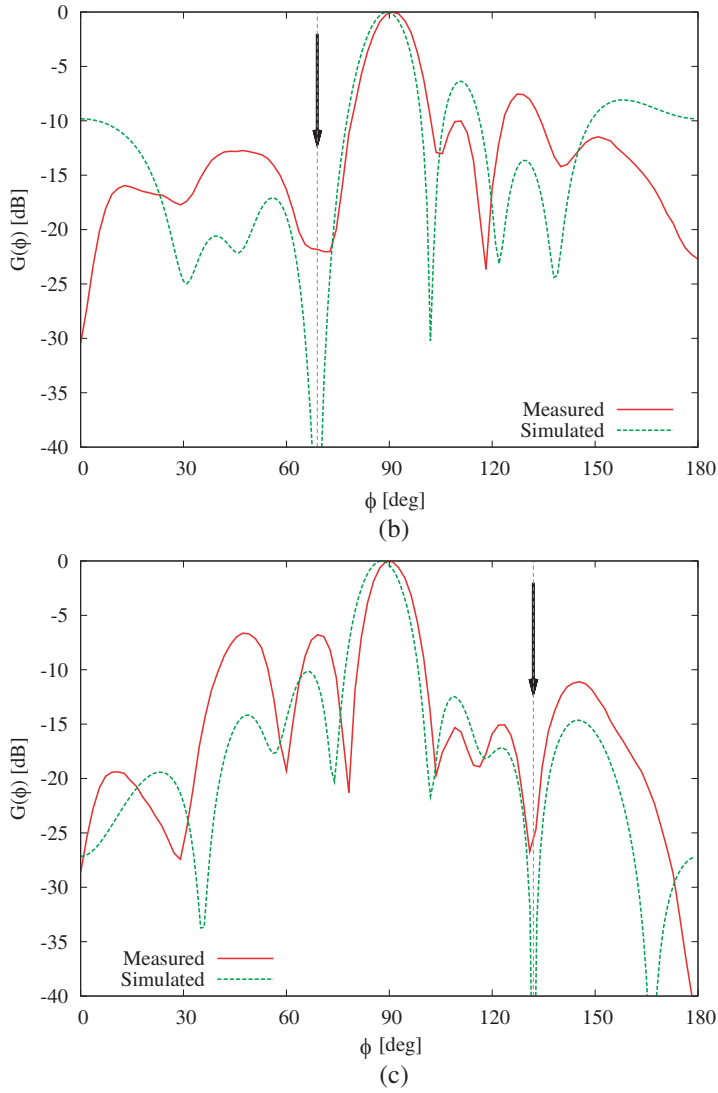


**Figure 5.** *Experiment A* — (a) Behavior of the *SINR* versus the iteration index $\chi$. Beam pattern synthesized at (b) $l = 1$ and (c) $l = 3$.

th iteration turning off both $d(\chi)$ and $u_q(\chi)$, $q = 1, \ldots, Q$. With reference to Fig. 5(a), the *SINR* black values measured at each time-step $t_l$, $l = 1, \ldots, L$ turn out to be always greater than 32 dB with a dynamics of about 10 dB [$SINR(t_1) = 33.86$ dB, $SINR(t_2) = 38.48$ dB,

$SINR(t_3) = 42.36\,\text{dB}$, $SINR(t_4) = 32.96\,\text{dB}$, and $SINR(t_5) = 34.86\,\text{dB}$]. As for the response of the PSO-driven software control module, the computation time required by each iteration is in the order of 1.6 ms on a CPU Intel P4, as also reported in [18]. For comparison purposes, the plot of the *SINR* simulated with the model in [18] is reported, as well. As it can be observed, there is an acceptable agreement between the two plots although some differences occurs since the model does not reproduce the actual structure of the antenna.[‡]

In order to give some indications of the effects of the *SINR* maximization on the antenna beamforming, some samples of the radiation pattern in correspondence with different time-steps are shown. More specifically, Fig. 5(b) shows the pattern shape at the step $l = 1$ [$SINR(t_1) = 33.86\,\text{dB}$] when the interference impinges on the array from $\phi^u = 69$ with a power equal to 150 mW. The measured beam pattern is characterized by a null of about $-22\,\text{dB}$ along the jammer direction $\phi = \phi^u$. A similar result is obtained at $l = 3$ for a jammer coming from the direction $\phi^u = 132$ with a lower power level ($\Psi^u = 80\,\text{mW}$) [Fig. 5(c)].

### *4.2.2. Experiment B*

In the second experiment, the interference scenario is characterized by $Q = 2$ undesired sources with the desired signal that impinges on the antenna from $\phi^d = 0$. Unlike the previous experiment, the power of jammers has been set to the same value of that of $d(t_l)$ (i.e., $\Psi^d = \Psi^u = 100\,\text{mW}$).

**Table 3.** *Experiment B* — Description of the interference scenario. Evolution of the *DoA*s and power levels of the interference signals.

| $l$ | $\phi_1^u(t_l)$ [deg] | $\phi_2^u(t_l)$ [deg] |
|---|---|---|
| 1 | 111 | 69 |
| 2 | 111 | 78 |
| 3 | 114 | 132 |
| 4 | 69 | 48 |

Although the *DoA*s of the interferences have been varied as in Table 3, the smart antenna is able to obtain *SINR* values at the receiver in the range $20.23\,\text{dB} \leq SINR(t_l) \leq 23.45\,\text{dB}$ [Fig. 6(a)]. As expected, the average *SINR* value reduces compared to

[‡] The numerical simulations are performed by considering an ideal array of point-like sources placed in front of an infinite reflecting plane at a distance of 0.25 wavelengths.

that of the previous experiment because of the presence of two undesired signals ($av_{l=1,\ldots,L}\{SINR(t_l)\}\rfloor_{\exp B} = 21.81\,\text{dB}$ vs. $av_{l=1,\ldots,L}\{SINR(t_l)\}\rfloor_{\exp A} = 36.46\,\text{dB}$). However, the radiation patterns are still characterized by nulls effectively located at $\phi_q^u(t_2) = \{111, 78\}$ [Fig. 6(b)] and $\phi_q^u(t_3) = \{114, 132\}$ [Fig. 6(c)] further confirming the conclusions on the interference rejection of the smart antenna prototype. More specifically, the nulls obtained with the PSO-driven control have the following depths: $G\{\phi_1^u(t_2)\} = -27\,\text{dB}$,

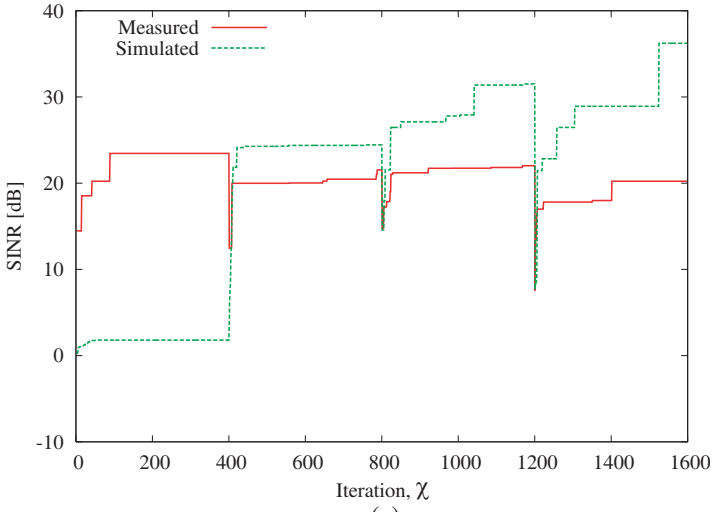


(a)

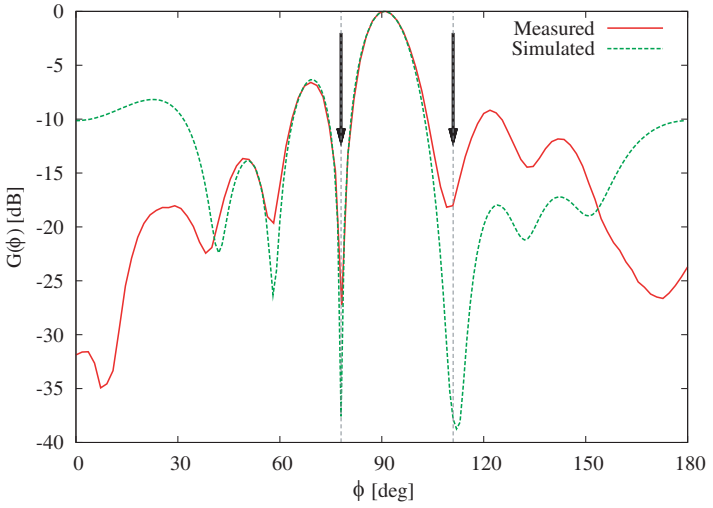


(b)

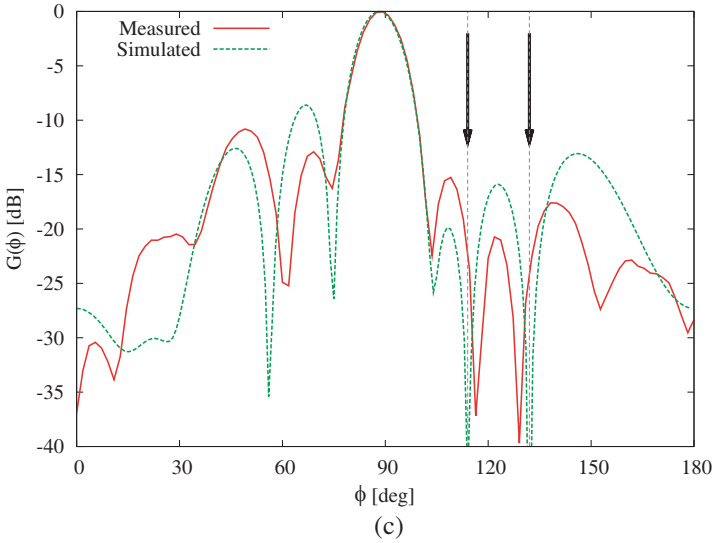


**Figure 6.** *Experiment B* — (a) Behavior of the *SINR* versus the iteration index $\chi$. Beam pattern synthesized at the time-steps (b) $l = 2$ and (c) $l = 3$.

$G\{\phi_2^u(t_2)\} = -17\,\text{dB}$ in the second time-step ($l = 2$) [Fig. 6(b)] and $G\{\phi_1^u(t_3)\} = -23\,\text{dB}$ and $G\{\phi_2^u(t_3)\} = -27\,\text{dB}$ at $l = 3$ [Fig. 6(c)].

Concerning the comparison between simulated and measured patterns, there is a good agreement about the positions of the nulls as well as on the pattern shape in the range $30 < \phi < 150$, while non-negligible differences occur in the other angular regions due to the limited dimensions of the measurement environment.

**Table 4.** *Experiment C* — Description of the interference scenario. Evolution of the *DoA*s and power levels of the interference signals.

| $l$ | $\phi_1^u(t_l)$ [deg] | $\phi_2^u(t_l)$ [deg] | $\phi_3^u(t_l)$ [deg] |
|---|---|---|---|
| 1 | 108 | 66 | 102 |
| 2 | 108 | 66 | 78 |
| 3 | 78 | 48 | 63 |
| 4 | 120 | 132 | 102 |

### *4.2.3. Experiment C*

The last experiment is concerned with the same setup of the *Experiment B* except for the number of interferers ($Q = 3$) and their DoAs as described in Table 4. The plot of the *SINR* versus the iteration index $\chi$ is shown in Fig. 7(a). As it can be observed, the range of the *SINR* is $12.17\,\text{dB} \leq SINR(t_l) \leq 21.08\,\text{dB}$ and the effectiveness of the interference suppression procedure is still assessed

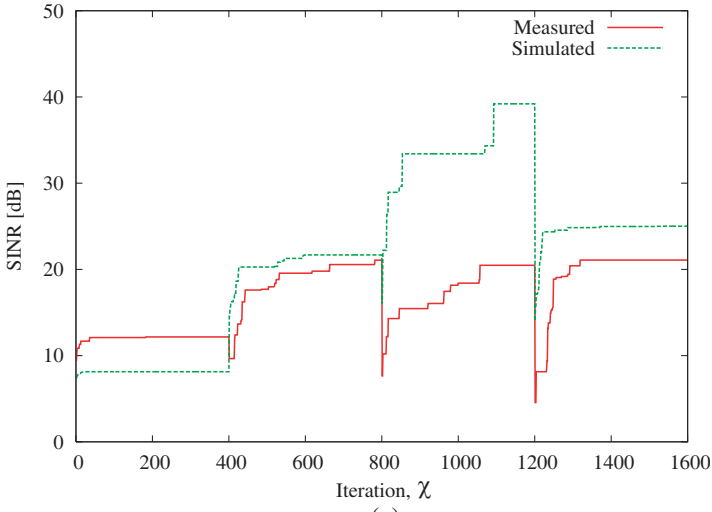


(a)

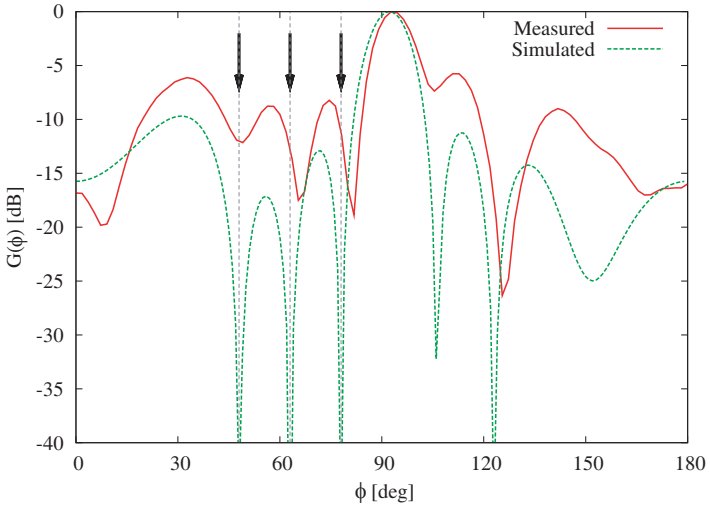


(b)

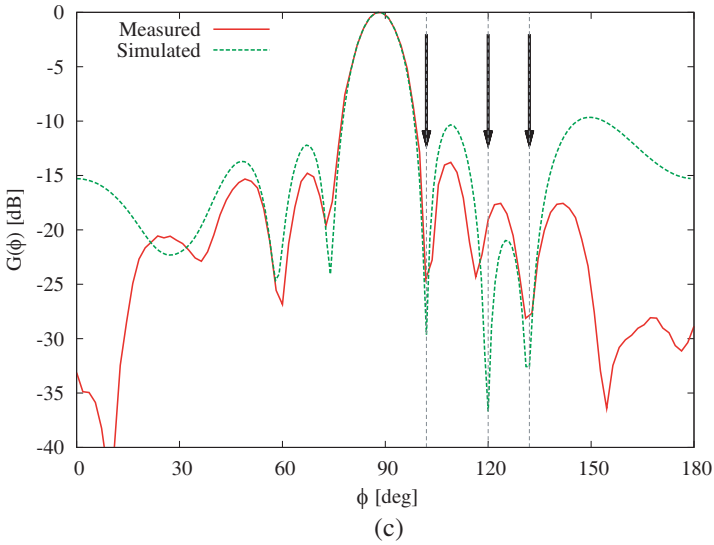


**Figure 7.** *Experiment C* — (a) Behavior of the *SINR* versus the iteration index $\chi$. Beam pattern synthesized at (b) $l = 3$ and (c) $l = 4$.

as confirmed by the pattern samples shown in Fig. 7(b) ($l = 3$) and Fig. 7(c) ($l = 4$). As regards $l = 3$, the measured locations of the nulls turn out to be close to the simulated ones even though they are not completely aligned to the DoAs of the undesired signals. However, the attenuation in correspondence with the jammers is always lower than 10 dB, since $G\{\phi_1^u(t_3)\} = -11$ dB, $G\{\phi_2^u(t_3)\} = -12$ dB, and $G\{\phi_3^u(t_3)\} = -12$ dB. On the contrary, Fig. 7(c) shows that, at the time-step $l = 4$, the nulls are effectively located along the directions $\phi_1^u(t_4) = 120$, $\phi_2^u(t_4) = 132$, and $\phi_3^u(t_4) = 102$, with a depth of $G\{\phi_1^u(t_4)\} = -24$ dB, $G\{\phi_2^u(t_4)\} = -20$ dB, and $G\{\phi_3^u(t_4)\} = -27$ dB, respectively.

## 5. CONCLUSION

In this paper, an experimental realization of a fully adaptive array has been discussed. The system is characterized by a simple architecture consisting of a radiating module, a HW control module, a power combiner, and a SW control module. The signal received at the array elements is suitably processed according to a PSO-based control strategy aimed at maximizing the SINR at the output the system. The experimental validation has demonstrated the feasibility of the

adaptive control as well as the reliability of the antenna prototype.

More specifically, the proposed implementation is characterized by

- a low-complexity and low-cost architecture able to shift the locations of the pattern nulls in a continuous way;
- capability of adaptively react to changing interference scenarios characterized by single and multiple jammers;
- capability of optimizing the system performance in terms of SINR values and suppression of the interferences.

As for future developments, they will be concerned with

- the analysis and a successive implementation of more realistic numerical models aimed at carefully modeling the non-ideal behavior of the array (e.g., non-ideal array elements, the presence of the reflecting plane, mutual coupling effects, etc..);
- the design and testing of more compact geometries useful for an integration in small size wireless devices (e.g., mobile stations and wireless sensor nodes).

## REFERENCES

1. Alexiou, A. and M. Haardt, "Smart antenna technologies for future wireless systems: Trends and challenges," *IEEE Comm. Mag.*, Vol. 42, 90–97, Sep. 2004.
2. Bellofiore, S., C. A. Balanis, J. Foutz, and A. S. Spanias, "Smart antennas systems for mobile communication networks. Part 1: Overview and antenna design," *IEEE Trans. Antennas Propagat.*, Vol. 44, 145–154, May 2002.
3. Bellofiore, S., J. Foutz, C. A. Balanis, and A. S. Spanias, "Smart antennas systems for mobile communication networks. Part 2: Beamforming and network throughput," *IEEE Trans. Antennas Propagat.*, Vol. 44, 106–114, May 2002.
4. Chryssomallis, M., "Smart antennas," *IEEE Antennas Propagat. Mag.*, Vol. 42, 129–136, Jun. 2000.
5. Godara, L. C., "Applications of antenna arrays to mobile communications, Part I: Performance improvement, feasibility, and system considerations," *Proc. IEEE*, Vol. 85, 1031–1060, Jul. 1997.
6. Murch, R. D. and K. B. Letaief, "Antenna systems for broandband wireless access," *IEEE Commun. Mag.*, Vol. 40, 76–83, Apr. 2002.

7. Piazza, D., N. J. Kirsh, A. Forenza, R. W. Heath, and K. R. Dandekar, "Design and evaluation of a reconfigurable antenna array for MIMO systems," *IEEE Trans. Antennas Propagat.*, Vol. 56, 869–881, Mar. 2008.
8. Applebaum, S. P., "Adaptive arrays," *IEEE Trans. Antennas Propagat.*, Vol. 24, 585–598, Sep. 1976.
9. Song, C. T. P., A. Mak, B. Wong, D. George, and R. D. Murch, "Compact low cost dual polarized adaptive planar phased array for WLAN," *IEEE Trans. Antennas Propagat.*, Vol. 53, 2406–2416, Aug. 2005.
10. Migliore, M. D., D. Pinchera, and F. Schettino, "A simple and robust adaptive parasitic antenna," *IEEE Antennas Propagat. Mag.*, Vol. 53, 3262–3272, Oct. 2005.
11. Donelli, M., R. Azaro, L. Fimognari, and A. Massa, "A planar electronically reconfigurable Wi-Fi band antenna based on a parasitic microstrip structure," *IEEE Antenna Wireless Propagat. Lett.*, Vol. 6, 623–626, 2007.
12. Celik, N., W. Kim, M. F. Demirkol, M. F. Iskander, and R. Emrick, "Implementation and experimental verification of hybrid smart-antenna beamforming algorithm," *IEEE Antenna Wireless Propagat. Lett.*, Vol. 5, 280–283, 2006.
13. Diop, M., J. F. Diouris, and J. Saillard, "A low-cost experimental adaptive array built in the UHF band (900 MHz) for a minimum response time in interference cancellation," *Proc. IEEE Vehicular Technology Conference*, 25–28, 1992.
14. Widrow, B., P. E. Mantey, L. J. Griffiths, and B. B. Goode, "Adaptive antenna systems," *Proc. IEEE*, Vol. 55, 2143–2159, Dec. 1967.
15. Haupt, R. L. and H. Southall, "Experimental adaptive cylindrical array," *Proc. IEEE Aerospace Conference*, 291–296, 1999.
16. Azaro, R., L. Ioriatti, M. Martinelli, M. Benedetti, and A. Massa, "An experimental realization of a fully-adaptive smart antenna," *Microw. Opt. Tech. Lett.*, Vol. 50, No. 6, 1715–1716, Jun. 2008.
17. Benedetti, M., R. Azaro, and A. Massa, "Experimental validation of a fully-adaptive smart antenna prototype," *Elect. Lett.*, Vol. 44, No. 11, 661–662, May 2008.
18. Benedetti, M., R. Azaro, and A. Massa, "Memory enhanced PSO-based optimization approach for smart antennas control in complex interference scenarios," *IEEE Trans. Antennas Propag.*, Vol. 56, 1939–1947, Jul. 2008.
19. Weile, D. S. and E. Michielssen, "The control of adaptive antenna

arrays with genetic algorithms using dominance and diploidy," *IEEE Trans. Antennas Propagat.*, Vol. 49, 1424–1433, Oct. 2001.

20. Compton Jr. R. T., *Adaptive Antennas*, Prentice Hall, Englewood Cliffs, NJ, 1988.
21. Godara, L. C., *Smart Antennas*, CRC Press, Boca Raton, FL, 2004.
22. Donelli, M., R. Azaro, F. De Natale, and A. Massa, "An innovative computational approach based on a particle swarm strategy for adaptive phased-arrays control," *IEEE Trans. Antennas Propagat.*, Vol. 54, 888–898, Mar. 2006.
23. Chuang, H.-R. and L.-C. Kuo, "3-D FDTD design analysis of a 2.4-GHz polarization-diversity printed dipole antenna with integrated balun and polarization switching circuit for WLAN and wireless communication applications," *IEEE Trans. Microw. Theory Tech.*, Vol. 51, 374–381, Feb. 2003.
24. Analog Devices, 1.5 GHz to 2.4 GHz RF vector modulator. One Technology Way, MA, 2004. [Online]. Available: www.analog.com/UploadedFiles/Data_Sheets/AD8341.pdf.
25. Pozar, D. M., *Microwave Engineering*, John Wiley, Hoboken, NJ, 2005.
26. Benedetti, M., P. Rocca, R. Azaro, and A. Massa, "A fully-adaptive smart antenna prototype: Numerical modeling and experimental validation," *Proc. 2008 IEEE AP-S International Symposium*, San Diego, CA, USA, Jul. 5–11, 2008.
27. Benedetti, M., G. Oliveri, M. Donelli, P. Rocca, and A. Massa, "Experimental validation of smart antenna system model," *Proc. 2009 IEEE AP-S International Symposium*, Charleston, SC, USA, Jun. 1–5, 2009.